Combustion and Flame 234 (2021) 111661

Contents lists available at ScienceDirect

Combustion and Flame

journal homepage: www.elsevier.com/locate/combustflame

End-gas autoignition fraction and flame propagation rate in laser-ignited primary reference fuel mixtures at elevated temperature and pressure

Andrew Zdanowicz[a], Jeffrey Mohr[a], Jessica Tryner[a], Kara Gustafson[a], Bret Windom[a], Daniel B. Olsen[a], Gregory Hampson[b], Anthony J. Marchese[a,*]

[a] Department of Mechanical Engineering, Colorado State University, 1301 Campus Delivery, Fort Collins, CO 80523, United States
[b] Woodward Inc., Loveland, CO 80538, United States

ARTICLE INFO

Article history:
Received 12 August 2019
Revised 2 August 2021
Accepted 3 August 2021

Keywords:
Engine knock
End-gas autoignition, rapid compression machine
Fuel reactivity
Octane number
CFD modeling

ABSTRACT

Knock in spark-ignited (SI) engines is initiated by autoignition of the unburned gasses upstream of spark-ignited, propagating, turbulent premixed flames. Knock propensity of fuel/air mixtures is typically quantified using research octane number (RON), motor octane number (MON), or methane number (MN; for gaseous fuels), which are measured using single-cylinder, variable compression ratio engines. In this study, knock propensity of SI fuels was quantified via observations of end-gas autoignition (EGAI) in unburned gasses upstream of laser-ignited, premixed flames at elevated pressures and temperatures in a rapid compression machine. Stoichiometric primary reference fuel (PRF; n-heptane/isooctane) blends of varying reactivity ($50 \leq PRF \leq 100$) were ignited using an Nd:YAG laser over a range of temperatures and pressures, all in excess of 545 K and 16.1 bar. Laser ignition produced outwardly-propagating premixed flames. High-speed pressure measurements and schlieren images indicated the presence of EGAI. The fraction of the total heat release attributed to EGAI (i.e., EGAI fraction) varied with fuel reactivity (i.e., octane number) and the time-integrated temperature of the end-gas prior to ignition. Flame propagation rates, which were measured using schlieren images, were only weakly correlated with octane number but were affected by turbulence caused by variation in piston timing. Under conditions of low turbulence, measured flame propagation rates approached one-dimensional premixed laminar flame speed computations performed at the same conditions. Experiments were simulated with a three-dimensional CONVERGE^{TM} model using reduced chemical kinetics (121 species, 538 reactions). The simulations accurately captured the measured flame propagation rates, as well as the variation in EGAI fraction with fuel reactivity and time-integrated end-gas temperature. The simulations also revealed low-temperature heat release as well as formaldehyde and hydrogen peroxide formation in the end-gas upstream of the propagating flame, which increased the temperature and degree of chain branching in the end-gas, ultimately leading to EGAI.

1. Introduction

The onset of knock is the foremost limitation constraining thermal efficiency in spark-ignited (SI) engines. Engine knock is initiated by uncontrolled autoignition of the unburned end-gasses upstream of the spark-ignited propagating flame [1]. End-gas autoignition (EGAI) is governed primarily by the reactivity of the fuel/air mixture, in-cylinder temperature, and length of time during which the end-gasses reside at elevated temperatures. Under normal engine operating conditions, the spark-initiated propagating flame consumes nearly all of the premixed fuel and air. Heat transfer to the walls of the cylinder maintains a cool thermal boundary layer that quenches the flame, and any remaining unburned gasses avoid undergoing autoignition as temperatures decrease during the expansion stroke. Under more severe operating conditions, the end-gasses are compressed and heated to a higher degree—ultimately reaching a critical chemical kinetic induction period as the slow initial combustion reactions in the end-gas transition to exponentially faster chain-branching reactions. Under these conditions, EGAI occurs – either locally or volumetrically – before the propagating flame can consume all of the unburned fuel/air mixture. Severe EGAI (i.e., engine knock) results in the breakdown of the thermal boundary layer that protects com-

* Corresponding author.
E-mail address: marchese@colostate.edu (A.J. Marchese).

https://doi.org/10.1016/j.combustflame.2021.111661
0010-2180/

ponents from direct exposure to combustion radicals and extreme temperatures, resulting in surface corrosion and potential component failure with time. To maximize durability, SI engines are designed to operate with compression ratio, boost pressure, and fuel reactivity constraints that avoid EGAI.

The conventional metrics used to quantify the propensity of an SI fuel to autoignite are the research and motor octane numbers (RON and MON) [2–4], along with methane number (MN) for gaseous SI fuels [5]. The RON and MON standards were developed to describe a fuel's resistance to knock and thus determine its suitability for a given engine and set of operating conditions. Specifically, the RON and MON standards represent a comparison of the tested fuel's critical compression ratio to that of a primary reference fuel (PRF) blend (n-heptane and isooctane) under standardized operating conditions in a Cooperative Fuels Research (CFR) engine - a single-cylinder, variable compression ratio engine.

Despite their apparent similarities, there is no direct correlation between the RON and MON metrics, as they represent the knock propensity of the test fuel at distinct end-gas conditions spanning the negative temperature coefficient (NTC) region of hydrocarbon fuels [6]. The extent to which they successfully represent the NTC physics of SI combustion has been questioned, as numerous researchers have found that the ON and MN metrics are less predictive of how fuels will behave in modern engine configurations [7–11]. Kalghatgi et al. proposed the use of an Octane Index (OI) [8] that could better describe a fuel's autoignition characteristics for a specific engine configuration. Other researchers have proposed similar alternatives for both liquid and gaseous fuels [12,13]. Still, given the complexity of the governing phenomena, summarizing a fuel's autoignition behavior across all engine platforms with a single metric remains a challenge.

Furthermore, there is a need for a knock propensity metric that can be measured without a single-cylinder research engine. Efforts to produce novel fuels (e.g., advanced biofuels) often yield very small, costly quantities, whose combustion properties need to be characterized at engine relevant conditions. Measurement of the fuel's octane number (or other proposed alternative) in the early stages of fuel development is often impractical due to the quantity of fuel required. Benchtop cetane number (CN) measurement instruments, like the ignition quality tester (IQT) and the fuel ignition tester (FIT) [14,15] exist to meet this need, but a standardized method for measuring ON (or other knock propensity metric) using small quantities of fuel has yet to be developed [12,16–18].

Several researchers have employed constant volume combustion apparatuses (CVCA) as a means to study autoignition. For example, Hu and Keck proposed the use of a CVCA to study autoignition events ahead of an SI premixed flame [19]. More recently, Lawson and coworkers have expanding on this work [20]. In these experiments, a propagating SI flame compresses and heats the unburned upstream gasses, which are eventually brought to their autoignition limits. The measured pressure-time history over the course of the experiment is used to derive an end-gas temperature-time history up to the point of autoignition. These data have proven to be highly valuable to kinetic model validation, but to our knowledge have not been used to quantify the autoignition propensities of the tested fuels. Further, the end-gas temperatures and pressures produced in SI CVCA experiments are considerably lower than what is relevant to the end-gasses in modern engines (and their time scales considerably longer).

Rapid compression machines (RCMs) can provide experimental conditions with higher temperatures and pressures than typical CVCA experiments and have been widely employed to study homogenous autoignition chemistry. Recently, researchers at several institutions have employed RCMs to perform SI experiments [21-23], and use these experiments to characterize SI combustion phenomena under engine relevant conditions. This study centers on exploring the potential to use an RCM operating in SI mode to characterize end-gas autoignition propensity.

The ideal autoignition-propensity measurement instrument would: (1) require small amounts of fuel, (2) allow for variable end-gas conditions (e.g., pressure, temperature, species consistent with exhaust gas recirculation), (3) include high-speed pressure measurement capability for apparent heat release rate calculation, (4) include optical access for EGAI observation and flame propagation rate measurements, and (5) be amenable to chemically reacting flow modeling with detailed chemical kinetics. An RCM has several advantages as an instrument for studying EGAI and knock propensity compared to conventional engine testing. Specifically, an RCM: (1) requires substantially less fuel than an engine (~0.25 mL/test), (2) can safely reach temperatures and pressures consistent with end-gas conditions in current and future engines, (3) is optically accessible, (4) can be more accurately modeled than an internal combustion engine because of precise knowledge of the initial conditions, and (5) can be designed to produce minimal turbulence in the flow field after compression [2,24].

Qi et al. used a single-piston RCM with a conventional spark plug to examine knock and superknock of stoichiometric isooctane/air mixtures at three different compression ratios [25]. More recently, Dumitrache et al. [21] developed a technique to produce a laser-generated spark in an opposed piston RCM. The advantage of the opposed-piston layout is that it can facilitate symmetrical compression events to create a stagnation condition at the center of the chamber where the laser-spark is formed. This embodiment allows for single-point ignition in a nearly quiescent, high-temperature, high-pressure, reactive gas volume, wherein the temperature and velocity gradients are minimized. Bhoite [24] performed CFD simulations with detailed chemical kinetics of the laser-ignited methane/air mixtures of Dumitrache et al. [21], which accurately captured initial flame propagation rates for methane/air mixtures at various equivalence ratios. Bhoite also performed CFD simulations of stoichiometric, laser-ignited PRF/air mixtures and those simulations predicted EGAI upstream of the propagating PRF/air flames in the RCM [24].

The goal of the present study was to perform a proof of concept for an alternative method for quantifying the autoignition propensity of SI fuels via observations of EGAI in the unburned gasses upstream of laser-ignited, premixed flames at elevated pressures and temperatures in an RCM. Primary reference fuel (n-heptane/isooctane) blends of varying reactivity ($50 \leq$ PRF ≤ 100) were ignited by a laser spark at the center of the combustion chamber in an opposed-piston RCM. High-speed pressure measurements and schlieren imaging were used to characterize the combustion processes, quantify the magnitude of the EGAI events, and measure flame propagation rates. To elucidate the underlying phenomena that led to EGAI, experimental results were compared against a transient, three-dimensional computational CONVERGE^{TM} model with a reduced PRF chemical kinetic mechanism (121 species, 538 reactions [26]).

2. Methods

2.1. Rapid compression machine and associated instrumentation

The opposed-piston rapid compression machine (RCM) used in this study was manufactured by Marine Technology, LTD of Galway, Ireland and was configured with a nominal compression ratio of 11.6:1 for all experiments described herein (see Fig. 1). The combustion chamber is heated externally to maintain a uniform initial temperature. Pneumatic bellows on the backside of the piston assemblies are charged to 200 psi with air to provide the compressive force. Upon firing, the test gas mixture in the combustion chamber is compressed in 15 to 25 ms. After compression, the

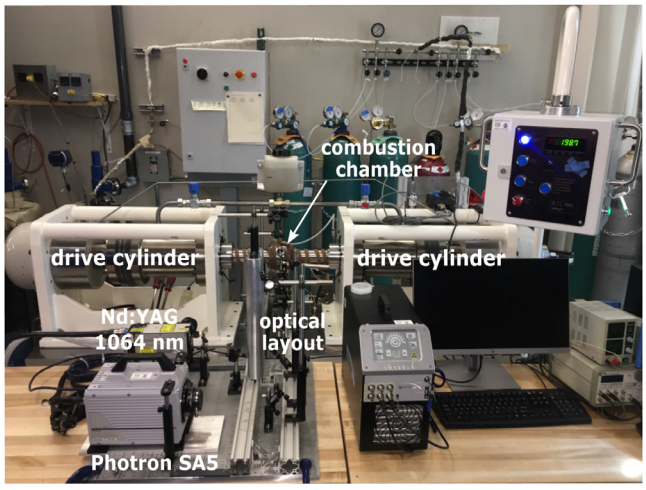

Fig. 1. A photograph of the rapid compression machine and its associated instrumentation.

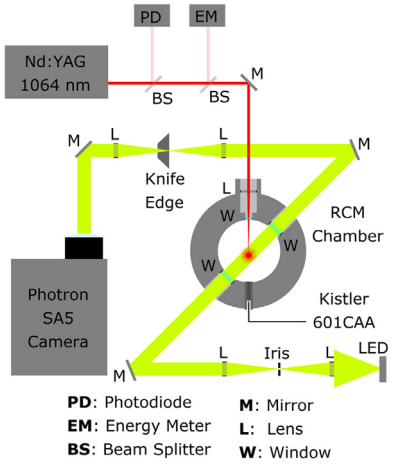

Fig. 2. Schematic diagram of the RCM optical layout. The Nd:YAG 1064 nm laser pathway shown in red. The schlieren collimated light pathway shown in green. (For interpretation of the references to color in this figure legend, the reader is referred to the web version of this article.)

pistons are held at top dead center (TDC) to maintain a constant volume of 30.0 cm^3 (diameter: 3.82 cm, length: 1.90 cm, crevice volume: 8.2 cm^3) for the remainder of each experiment. Creviced pistons are used to mitigate the effects of roll-up vortices, and thereby minimize fluid dynamic disturbances and the convection of cooler gasses from the boundary layer into the near-adiabatic gas core [27].

A laser-generated spark is used to ignite the gas mixture in the center of the adiabatic core 10 ms after the pistons reach their TDC positions. The optical layout for the laser ignition system is shown in Fig. 2. A pulse-delay generator, triggered by the rise in pressure due to compression, is used to fire a 1064 nm, Q-switched, Quantel Q-smart100 Nd:YAG laser with a pulse energy of 35 mJ. The laser passes through a beam splitter that diverts ~5% to a photodiode used to measure the relative timing of the laser spark and compression event. A second beam splitter diverts a portion of the remaining beam to an Ophir PE25BF energy sensor to indirectly measure the energy delivered to the combustion chamber via the spark. The remainder of the beam (~90%) passes through a converging plano-convex lens just before entering the combustion chamber. The laser-induced spark is formed at the focal point of the lens, aligned to the center of the chamber. More information about the integration of the RCM and laser ignition system can be found in Dumitrache, et al. [21].

The pressure inside the RCM combustion chamber is measured using a thermally-compensated pressure transducer (Kistler 601CAA). Pressure data are recorded along with ignition timing using a Picoscope 4424 data acquisition system with a sample rate of 2 MHz. Schlieren imaging is used to optically observe combustion phenomena and measure flame propagation rate. The optical layout for the schlieren imaging system is also shown in Fig. 2. Light from a 405 nm LED is collimated through a series of lenses and mirrors and then directed through the two opposed sapphire windows (16.1 mm diameter) in the combustion chamber. After passing through the gas medium, light is focused to a point and split by a knife edge. The light is re-collimated and collected by a high-speed Photron SA5 camera operating at 50,000 frames per second with a resolution of 155 pixels/mm^2.

2.2. Mixture formation and TDC condition control

Liquid isooctane and n-heptane were blended with inert and oxidizing gasses in a mixing tank as described by Boissiere [29]. The 19.23 L tank was evacuated prior to filling. Fuels were proportioned by their liquid volumes and evaporated upon being injected into the evacuated tank. gasses were added in succession, proportioned by partial pressure and tank temperature. All experiments were performed with the fuel and oxidizer components in stoichiometric proportion. The fuel blends were designated by PRF number (e.g., PRF 80 was composed of 80% isooctane and 20% n-heptane by mole). External tank heaters were set to 42 °C to prevent condensation and an internal stir bar was used to mix the gasses for a minimum of 2 h prior to filling the RCM combustion chamber.

The initial external temperature of the RCM chamber was maintained at 300 +/- 2 K for all experiments. The thermodynamic conditions after compression were controlled by adjusting the initial pressure and/or varying the ratio of specific heats of the test gas mixture by varying the inert gas blend. Specifically, an inert blend of nitrogen and carbon dioxide was used to lower the ratio of specific heats of the test gas blend. The oxidizer/inert gas blends and initial pressures investigated were designated by experiment index, as listed in Table 1. The temperatures and pressures listed in Table 1 represent the full range of experimental observations for the specified initial conditions. The temperature history during the compression process (up to and including TDC) was estimated using the ideal gas law with the known gas composition, the initial temperature, the pressure versus time data, and the specific volume versus time data.

Central to an RCM's design and utility in conducting fundamental combustion studies is a core volume within the combustion chamber assumed to undergo adiabatic compression (i.e. the "adiabatic core"). The adiabatic core assumption is satisfied reasonably well through the use of creviced pistons (for which a detailed account is provided in [28]) though challenges remain. Sung and Curran describe the "facility effect" [28], in which the fluid dynamic and heat transfer characteristics of each RCM not only cause a deviation from the adiabatic core assumption, but also cause significant variation in the temperature/time histories of the compression events among the numerous RCMs employed by combustion researchers across the globe. The lack of standardization of both machine construction and result interpretation methodology presents a challenge to interlaboratory RCM comparisons as well as the use of RCMs for chemical kinetic mechanism validation. For the proof-of-concept study on EGAI presented herein, the lack of standardization in RCM design and construction is less problematic. However, it is recognized that development of a standardized test method using a laser-ignited RCM to quantify knock propensity of SI fuels

Table 1
The six sets of test conditions used in this study. For experiment indices 1–3, thermodynamic conditions were altered by adjusting the initial pressure prior to compression. For indices 4–6, conditions were altered by adjusting the inert composition. All experiments were performed with stoichiometric fuel/oxidizer blends. Physical changes were made to the combustion chamber fill valve during the tests performed under experiment index 5. These changes increased the compression ratio from 11.6:1 to 11.9:1. Initial pressure was lowered to achieve similar TDC conditions to those of experiment index 4.

Index	Initial Pressure	Oxidizer/Inert Blend Composition (mole%)			Compression Ratio	TDC Temp. Range	TDC Press. Range
	(bar)	O_2	N_2	CO_2	(-)	(K)	(bar)
1	1.000 ± 0.001	21%	79%	–	11.6:1	729 - 887	24.9 - 27.8
2	0.900 ± 0.001	21%	79%	–	11.6:1	730 - 867	22.7 - 25.7
3	0.750 ± 0.001	21%	79%	–	11.6:1	725 - 873	18.8 - 22.9
4	1.000 ± 0.001	21%	67.1%	11.9%	11.6:1	698 - 829	24.4 - 26.2
5	0.975 ± 0.075	21%	67.1%	11.9%	11.9:1	702 - 817	24.5 - 25.8
6	1.000 ± 0.001	21%	39.5%	39.5%	11.6:1	691 - 775	23.2 - 24.4

would require the development of a standardized RCM configuration for this use.

The pneumatically-fired, opposed-piston RCM employed in this study is subject to compression asymmetries caused by differences in the static friction acting on the pistons and their circumferential seals between the two sides of the machine. Piston velocity is largely unaffected by these differences, but the timing offset between when the pistons are released relative to one another varies between experiments. Fluid dynamic and thermodynamic conditions at TDC proved sensitive to this "piston timing offset" as evidenced by the variation in measured pressure history and associated computed temperature history between TDC and spark ignition.

Table 1 exemplifies the variation of thermodynamic conditions after compression with initial conditions held constant. For example, Index 1 represents experiments performed with a starting pressure of 1.000 +/- 0.001 bar and temperature of 300 +/- 2 K, for which the calculated TDC temperatures varied from 729 to 887 K – a substantial range given the consistency of the initial conditions. While development of a future standardized RCM to quantify autoignition propensity would require a more controllable temperature history, the variations observed in the experiments enabled us to explore both the effect of fuel reactivity (in the form of ON of primary reference fuels) and end-gas temperature history prior to spark ignition by "binning" experiments not by their initial conditions in Table 1, but rather by their piston offset and time-integrated temperature (see Supplementary Information (SI) §S1.1).

The time-integrated temperature (Θ) was evaluated by integrating, with respect to time, the calculated bulk mean temperature of the gasses in the combustion chamber during the 10 ms interval prior to spark ignition:

$$\Theta = \int_{-10\ ms}^{0} T_m dt \tag{1}$$

where T_m is the calculated bulk-mean temperature in K and t is the time in s. The time-integrated temperature is known to govern the chemical kinetic induction period of the end-gas [30], and as discussed in §S3.3, the piston offset affects the level of turbulence into which the SI flames are initiated, thereby affecting their propagation rates. Binning the experiments in this manner treats the conditions after compression as the independent variables to which the dependent variables (i.e. the observed combustion characteristics) are compared. As discussed below, this approach provides the proof-of-concept for a future development of a standardized SI RCM with improved consistency that could be used to quantify knock propensity of fuels.

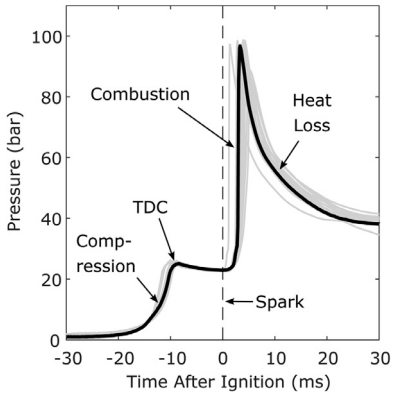

Fig. 3. Example pressure measurements for laser-ignited RCM experiments with the same initial conditions and fuel reactivity (index 1, PRF 50). The dark black line is a representative trial selected from the group of replicates, shown in gray. The pressure data are temporally aligned such that ignition occurs at time 0 for all trials shown. (For interpretation of the references to color in this figure legend, the reader is referred to the web version of this article.)

2.3. Data Interpretation and EGAI fraction evaluation

Selected PRF 50 (index 1) pressure histories for the laser-ignited RCM experiments are shown in Fig. 3. The rise in pressure before time 0 is due to the compression process. The pistons reach TDC at approximately −10.0 ms. The laser ignition system produces a spark in the center of the chamber at time 0, and the subsequent rise in pressure is due to combustion, which occurs via an outwardly propagating flame followed by autoignition of the end-gas upstream of the propagating flame. The decrease in pressure after combustion is due to heat transfer, rather than an expansion stroke.

The high-speed pressure data were used to calculate the apparent heat release rate (AHRR), in W, during the constant-volume combustion event as shown in Eq. (2) [1]:

$$AHRR = \frac{dQ}{dt} = \frac{1}{\gamma - 1} V \frac{dP}{dt} \tag{2}$$

where V is the gas volume after compression in m^3, γ is the ratio of specific heats of the mixture, P is the pressure in Pa, and t is the time in s. Note that dQ/dt represents the net rate of external heat addition to the gasses in the combustion chamber that would result in the measured pressure rise dP/dt due to conversion of chemical energy to thermal energy in a homogeneous chemically reacting system. The specific heat ratio of the mixture varied over the course of each experiment and was calculated at each sample point as a function of the estimated temperature and initial mixture composition, using empirical correlations for the mixture

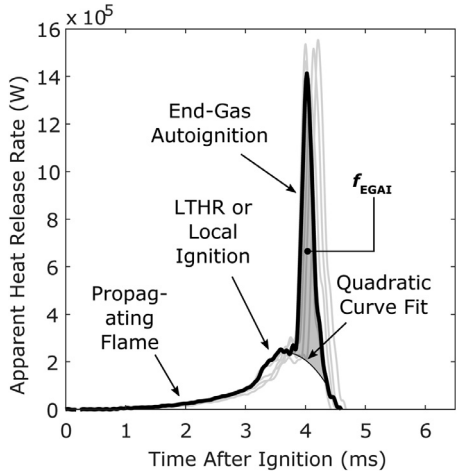

Fig. 4. Apparent heat release rate derived from pressure data for a PRF 90, index 1 test condition. Replicate trials shown in gray. A quadratic curve fit was calculated using the AHRR data before and after the EGAI peak to approximate the amount of energy released by the propagating flame. The EGAI fraction, f_{EGAI}, is the fraction of the total AHRR attributed to the autoignition event and is represented by the shaded region. The intermediary increase in AHRR prior to EGAI is likely caused by a local secondary ignition site or low temperature heat release in the end-gas upstream of the propagating flame. (For interpretation of the references to color in this figure legend, the reader is referred to the web version of this article.)

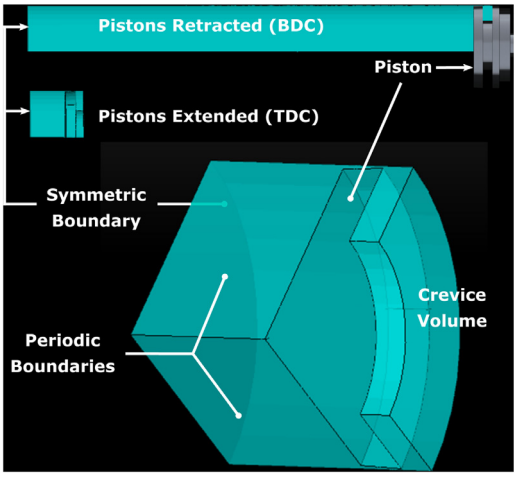

Fig. 5. Diagram of computational domain, which consists of a 1/8th sector of the RCM combustion chamber with periodic boundary conditions at the boundary of each sector and a symmetric boundary condition at the centerline of the combustion chamber. The diagram also indicates the crevice volume and the total volume before and after compression.

constituents [31]. Changes in species concentrations during combustion were not accounted for.

An example AHRR profile is shown in Fig. 4 to illustrate the procedures used to identify the combustion mode and quantify the fraction of the total apparent heat release attributed to the EGAI event. Distinct combustion modes—propagating flame, low-temperature heat release in the end-gas, and end-gas autoignition—were identified by their AHRR signatures as shown. The contribution of the EGAI event to the total apparent heat release was isolated by deconvolution of the AHRR curve. A quadratic function was fit to the data before and after the EGAI peak to estimate the portions of heat release attributed to the propagating flame and the EGAI event. The heat release during EGAI was evaluated as the integral of the isolated EGAI AHRR profile (i.e., the area between the AHRR curve and quadratic fit function).

We defined the EGAI heat release fraction (f_{EGAI}) as follows:

$$f_{EGAI} = \left[\int \frac{dQ}{dt}\right]_{EGAI} / \left[\int \frac{dQ}{dt}\right]_{Total} \quad (3)$$

where dQ/dt is the apparent heat release rate in W. The numerator represents the integrated apparent heat release during EGAI in J, and the denominator represents the total integrated apparent heat release in J.

2.4. Estimation of flame propagation rate

Schlieren images, collected in sequence, were used to measure the projected flame area for each image, which yielded an equivalent flame radius as a function of time (see SI §S1.2). A second-order polynomial was fit to the equivalent flame radius versus time data. Then, flame stretch effects were eliminated through the nonlinear extrapolation of Kelley and Law [32,33] to yield the zero-stretch flame propagation rate with respect to the burned gasses according to Eq. (4):

$$s_b = s_b^0 t + c r_f + 2L_b \ln\left(r_f\right) - 4\frac{L_b^2}{r_f} - \frac{8}{3}\frac{L_b^3}{r_f} \quad (4)$$

where s_b is the burned propagation rate approximated with the second-order polynomial in cm/s, s_b^0 is the zero-stretch burned propagation rate to be found in cm/s, t is time in s, c is a measurement constant, r_f is the equivalent spherical flame radius in cm, and L_b is the Markstein length in cm. While, strictly speaking, Eq. (4) is only valid for laminar, spherical flames, the correction was applied to all measured flame propagation rates to demonstrate that the measured stretch-corrected flame propagation rates approach the predicted laminar flame speed as piston timing offset (and associated turbulence) approach zero. The extrapolated zero-stretch burned flame propagation rate was converted to an unburned flame propagation rate by correcting for the change in density across the flame front using equation Eq. (5) [33].

$$s_u = s_b\left(\frac{\rho_b}{\rho_u}\right) \quad (5)$$

where s is the flame propagation rate in cm/s, ρ is the region density in kg/m^3, and the u and b subscripts represent the unburned and burned regions across the flame respectively. Unburned density was calculated using the initial pressure and known compression ratio. Burned density was approximated using the ideal gas law and the burned temperatures and molecular weight of the combustion products as predicted by 1-D CHEMKIN flame speed simulations with reduced chemical kinetics [22]. Additional information on the methods used to estimate the flame propagation rate is provided in SI §S1.2.

2.5. Computational modeling

Transient, three-dimensional CFD simulations of the RCM experiments were performed using CONVERGE^{TM} version 2.4.0 with SAGE combustion and κ-ε RANS turbulence models. A 121-species, 538-reactions reduced chemical kinetic mechanism, developed for primary reference fuels, was used to model the combustion kinetics [26]. These simulations were used to elucidate characteristic AHRR behavior observed in the experiments and to analyze the role of low temperature chemistry and radical formation in the end-gas prior to the EGAI event.

Given the axisymmetric geometry of the RCM system, the experiments were modeled in CONVERGE^{TM} using a 1/8th sector of the RCM combustion chamber with a symmetric boundary condition at the centerline, as depicted in Fig. 5. The symmetric boundary limited the model to cases with perfectly symmetrical compression events (i.e., no piston offset) but reduced computational

expense considerably. A base 4 mm cubic mesh was generated automatically for the domain by the CONVERGE™ software and was refined as needed with adaptive mesh refinement (AMR), grid scaling, and fixed embedding techniques. AMR was employed in areas with high temperature and velocity gradients and in regions in which the autoignition precursor species, formaldehyde (CH_2O) and hydrogen peroxide (H_2O_2), were produced. The fixed embedding technique was used along the wall of the chamber to resolve the boundary layer and simulate heat loss to the wall. A forced quench condition at the crevice volume inlet was employed in the model in accordance with experimental findings.

Because simulated combustion events were sensitive to the temperature history of the compression event prior to ignition, the compression profile for a single experimental trial was selected for modeling. The laser spark was simulated as a spherical thermal hotspot of 1.0 mm diameter and 5000 K at the center of the chamber. This hotspot was initiated 10 ms after the pistons reached TDC, consistent with experiments. No plasma kinetics were included in the simulated laser spark. Previous modeling of laser-ignited methane/air mixtures in the RCM indicated that qualitative agreement with experimental flame propagation rates, pressure history, and AHRR can be achieved without including plasma kinetics [24].

Simulations were performed for the PRF 50, PRF 80, and PRF 100 blends with initial pressure and inert composition defined by index 1 of Table 1. Temperature was initialized at 300 K and 328 K to impose two time-integrated temperature TDC conditions, $\Theta = 5.88$ Ks and $\Theta = 6.42$ Ks. Given the symmetrical compression condition imposed by the model, piston offset was fixed at 0 ms. All simulations were performed with the fuel and oxidizer blends in stoichiometric proportion.

One-dimensional, planar, premixed flame speed simulations were performed using CHEMKIN for comparison with the propagation rates measured in the experiments. Ambient conditions were initialized at 590 K and 22.5 bar—in accordance with typical temperatures and pressures observed at the time of ignition for index 1 experiments (see Table 1). The CHEMKIN simulations were performed using the mixture-averaged transport model and the same 121-species, 538-reaction PRF mechanism used in the CONVERGE simulations [26]. As discussed below, these computations suggest that as piston timing offset approaches 0 ms, the measured flame propagation rates approach the predicted laminar flame speed. The computations also suggest the presence of turbulence in experiments with increased levels of piston timing offset.

3. Results

3.1. Pressure, apparent heat release rate, and end-gas autoignition fraction measurements

The TDC thermodynamic conditions (as indicated by the time-integrated temperature) and fluid dynamic conditions (as indicated by the piston offset) for the full data set are shown in Fig. 6. Although turbulence intensity was not quantified, schlieren images clearly indicated that experiments with larger piston offset had increased convective velocity in the flow field after TDC. However, the data in Fig. 6 indicate that the time-integrated temperature did not correlate with piston offset. In the discussions that follow, time-indicated temperature, piston offset, and octane number are taken to be the independent variables to which the dependent variables (e.g. f_{EGAI}, flame propagation rate) are compared.

Data point proximity in Fig. 6 indicates the similarity of the time-integrated temperature and fluid motion conditions between experiments. In the discussion that follows, four separate regions—A, B, C, and D—were arbitrarily selected to capture data points with similar TDC conditions that spanned the full range of tested fuel reactivity. Regions A, B, and C were selected to capture the effects of variation in time-integrated end-gas temperature on the laser-ignited RCM experiments. Region D was selected to maintain similar thermodynamic and fluid dynamic conditions while investigating the effect of changing fuel reactivity on combustion phenomena. More information on the how the results presented herein vary as a function of the selected mean and range of time-integrated temperature and piston offset can be found in SI §S2.1.

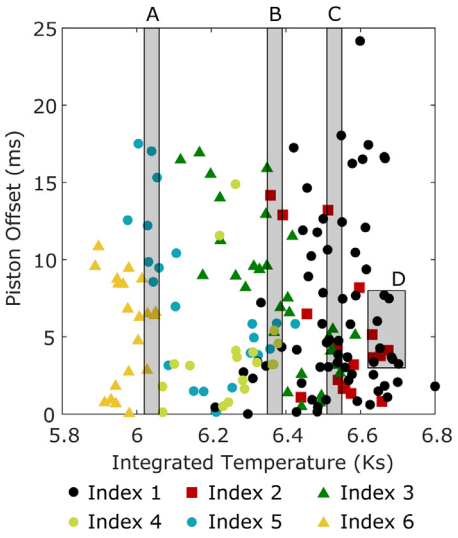

Fig. 6. The TDC conditions of the entire data set, as represented by the time-integrated temperature and piston timing offset of the compression events. Different symbols correspond to the initial condition indices listed in Table 1. Each data point represents a single experiment. All of the fuel blends are included in the figure. Time-integrated temperature indicates the temperature history after compression and prior to ignition. The A, B, C, and D shaded regions illustrate the TDC conditions selected for the data presented in Figs. 7-9. Data points that fall within the shaded regions meet the selection criteria and are said to have been subjected to similar conditions upon compression.

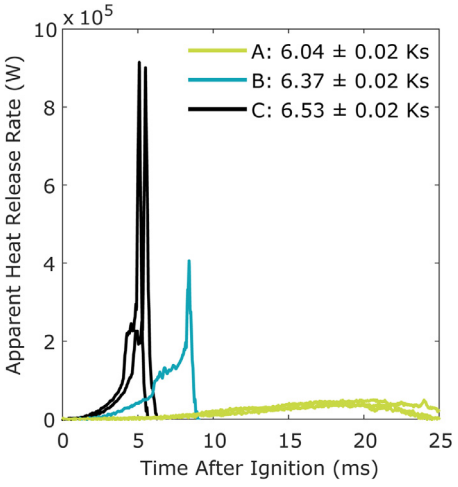

Fig. 7. AHRR profiles for PRF 100 experiments featuring time-integrated temperatures of 6.04 ± 0.02 Ks, 6.37 ± 0.02 Ks, and 6.53 ± 0.02 Ks (regions A, B, and C in Fig. 6). All replicate trials for all initial condition indices are shown.

AHRR results for the PRF 100 experiments with time-integrated temperatures of 6.04 ± 0.02 Ks, 6.37 ± 0.02 Ks, and 6.53 ± 0.02 Ks (i.e. regions A, B, and C in Fig. 6) are plotted in Fig. 7. It should be noted from Eq. (1), that these values of time-integrated temperature represent integrated average temperatures of 604 ± 2 K, 637 ± 2 K, and 653 ± 2 K, respectively. The magnitude of the maximum AHRR for the PRF 100 fuel blend increased substantially with the time integrated temperature. The lower time-integrated temperature experiments of Region A feature longer combustion

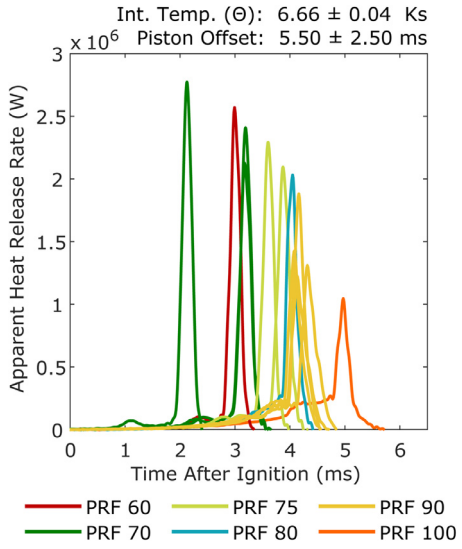

Fig. 8. AHRR profiles of experiments featuring time-integrated temperatures of 6.66 ± 0.04 Ks and piston offsets of 5.50 ± 2.50 ms (region D in Fig. 6). The colors of the AHRR curves indicate the octane number. All replicate trials within the selected range of time-integrated temperature and piston offset are included.

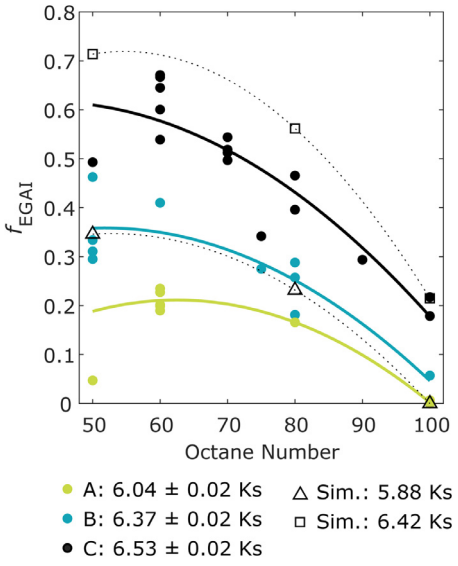

Fig. 9. EGAI fraction (f_{EGAI}) measurements plotted against ON for Θ = 6.04 ± 0.02 Ks, 6.37 ± 0.02 Ks and 6.53 ± 0.02 Ks and all piston offsets (i.e. regions A, B, and C in Fig. 6). Each symbol represents an individual test replicate. Second order polynomials were fit to the data using the least squares method. Simulation data for the Θ = 5.88 Ks and 6.42 Ks compression conditions are included for discussion in §3.4.

durations with no discernable EGAI signatures. The higher time-integrated temperature experiments of Regions B and C exhibit a period of moderate AHRR followed by a dramatic change in the slope. Such behavior is indicative of an initial period in which heat release produced by the spark-initiated propagating flame compressed the upstream unburned end-gasses and subsequently triggered EGAI.

The flame propagation rate, and therefore EGAI timing, was dependent on the flow field conditions at TDC. Region D of Fig. 6 includes selection criteria for both time-integrated temperature and piston offset to facilitate comparison of the combustion characteristics of fuels with varying ON. AHRR profiles of experiments with time-integrated temperatures of 6.66 ± 0.04 Ks and piston offsets of 5.50 ± 2.50 ms (i.e., Region D in Fig. 6) are plotted in Fig. 8. For a given time-integrated temperature, the delay between spark-ignition and EGAI decreased and the magnitude of the EGAI event increased as ON decreased. As fuel reactivity increased (with decreasing ON), the chemical kinetic induction period in the end-gas decreased, which resulted in earlier EGAI, a larger volume of autoignited gas and, therefore, a higher magnitude in apparent heat release during the EGAI event.

Fig. 9 includes the end-gas autoignition fraction, $f_{EGAI,}$ for all experiments with time-integrated temperatures of 6.04 ± 0.02 Ks, 6.37 ± 0.02 Ks, and 6.53 ± 0.02 Ks, respectively (i.e., Regions A, B and C in Fig. 6). The fraction of the total apparent heat release attributed to EGAI was lower for experiments with lower time-integrated temperature and lower fuel reactivity (i.e., higher ON). Piston offset did not strongly influence f_{EGAI} despite its direct correlation with flame propagation rate (see §3.3). The magnitude of an EGAI event is determined by the outcome of a competition between the propagation rate of the premixed flame and the chemical kinetic induction period for the autoignition chemistry in the end-gas. The amount of reactants that the propagating flame can consume prior to EGAI decreases as the autoignition delay period decreases. One might expect a larger piston offset and higher flame propagation rate to result in a lower f_{EGAI}. However, the end-gasses are also compressed and heated by the approaching flame. As a result, a higher flame propagation rate leads to higher temperatures and reaction rates in the end-gas (which decrease the autoignition delay period), which promotes EGAI and diminishes the correlation between propagation rate and f_{EGAI}. More information regarding the influence of flame propagation rate on EGAI is included in §S2.3 of the SI.

The magnitude of the EGAI fraction is also governed by the complexities of low temperature chemical kinetics in the end-gas. The PRF blends tested in this study clearly exhibited low temperature chemistry resulting in two-stage ignition behavior, as evidenced by the existence of local maxima in AHRR prior to the primary EGAI peak. This is most clearly depicted in the AHRR profiles of the higher reactivity blends in Fig. 8. Note that it is conceivable that low-temperature heat release could occur prior to the introduction of the spark but, in this study, such cases were identified as exhibiting “preignition” and were eliminated from the dataset for simplicity. The EGAI fraction, which is governed by a competition between the propagation rate of the premixed flame and chemical kinetic induction period of the end-gas is also subject to negative temperature coefficient (NTC) chemistry. Specifically, it is conceivable that, under some conditions (e.g. for lower time-integrated temperature and fuels with stronger NTC behavior), the increased temperature caused by the compression from the approaching flame could slow down the chemical kinetic induction of the end gas, thereby allowing the flame to penetrate further into the end-gas prior to EGAI. Such behavior could explain the non-linearity observed in the EGAI fraction with decreasing octane number at lower octane numbers observed in Fig. 9.

Further contributing to the apparent asymptotic behavior in EGAI fraction with decreasing octane number shown in Fig. 9 is related to definition of EGAI fraction and the behavior of fuels with low temperature reactivity in general. In principle, the upper limit of the f_{EGAI} metric is 1.0, which would constitute homogeneous charge compression ignition (HCCI; or very rapid spark-initiated HCCI) of the entire fuel/air mixture. However, fuels that exhibit two-stage ignition behavior can never achieve an EGAI fraction of 1.0 (as it is defined in Eq. (3) and depicted in Fig. 4) because a finite fraction of the fuel is consumed by the first-stage low temperature heat release. For all fuels and time-integrated temperature conditions considered in this study (experimentally and computationally), the highest value of f_{EGAI} observed was 0.70.

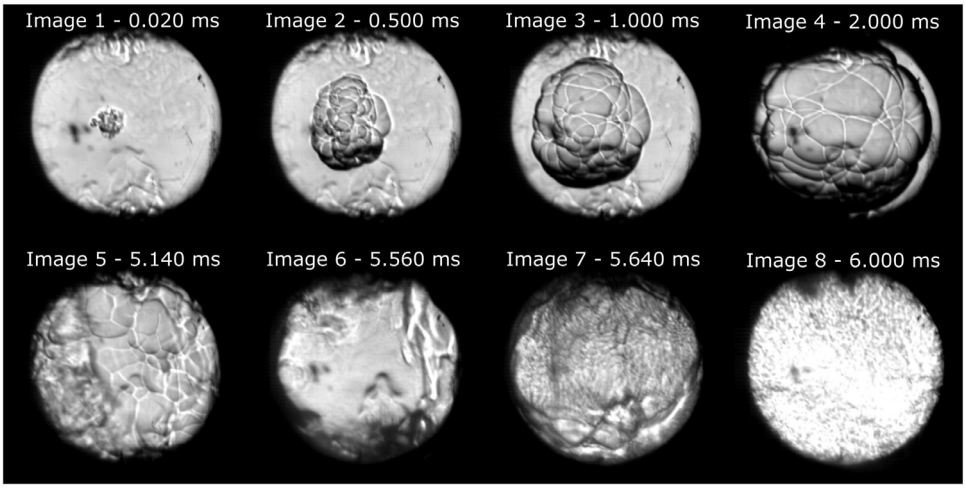

Fig. 10. Schlieren images captured at 50,000 frames per second for a PRF 90, index 3 experiment. Image numbers correspond with the labeled vertical dashed lines on the AHRR profile shown in Fig. 11. The time listed for each image is relative to the ignition timing.

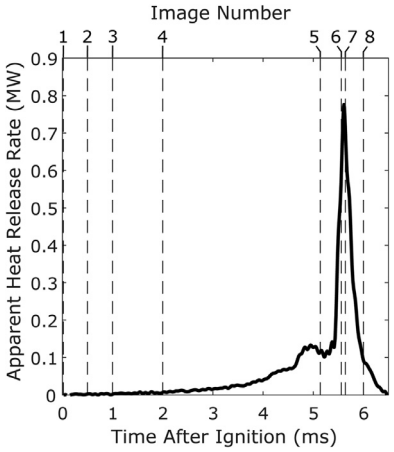

Fig. 11. AHRR profile for the PRF 90, index 4 experiment featured in the schlieren images of Fig. 10. Vertical dashed lines indicate the times at which those images were taken.

3.2. Optical observations of EGAI

Select schlieren images from a PRF 90, index 3 experiment with $\Theta = 6.44$ Ks and a piston offset of 0.496 ms are shown in Fig. 10. This trial was selected for the clarity with which the EGAI event was captured. The AHRR profile obtained during this experiment is shown in Fig. 11 and the time at which each image from Fig. 10 was obtained is indicated by the vertical dashed lines on Fig. 11. The first four images depict early-stage flame propagation. Ignition is captured in Image 1, immediately after the visible spark discharge. The flame kernel grows outward in the subsequent images and extends beyond the field of view in Image 4. Note that the field of view is limited by the relative size of the windows (16.1 mm diameter) to the size of the combustion chamber (19.0 mm distance between pistons at TDC; 38.2 mm bore). By the time the flame reaches the field of view boundary, it encompasses a mere 7% of the total chamber volume. Beyond this point, growth of cellular instabilities on the outer surface of the flame provide evidence for continued propagation. A low magnitude local peak in AHRR is detected just before 5 ms and, shortly after 5 ms, a secondary combustion event appears in the field of view on the left-hand side (image 5). This secondary combustion is indicative of low-temperature heat release (LTHR) and subsequent negative temperature coefficient (NTC) behavior in the end-gas as the AHRR decreases momentarily before the EGAI peak. Shortly thereafter, in Image 6, a sudden change in the schlieren image suggests that EGAI has occurred. The cellular instabilities that were present in flame front rapidly disappear and are replaced by a more uniform image that corresponds temporally to the primary EGAI peak in the AHRR curve. Images 7 and 8 were taken after peak AHRR and are indicative of convection of hot combustion products (and thermal radiation from particulate matter).

Synchronization with the AHRR profile suggested that schlieren images captured the presence of low-temperature volumetric heat release (LTHR) in the end-gas upstream of the propagating flame, which increased the temperature and produced stable combustion intermediates such as H_2O_2 and CH_2O prior to EGAI (as shown computationally in Figs. 15 and 16 below). We hypothesize that, as low-temperature reactions occur, the optical properties of the end-gas are affected by the temperature rise and presence of intermediate species. Optically, such events manifest themselves as distortions of the field of view and a sudden darkening or lightening of the image while the cellular structure of the flame surface remains visible. This effect is difficult to present in still image form, and is not readily distinguishable in the images of Fig. 10. Readers are encouraged to view the supporting video files provided as Supporting Information in §S2.2. Future improvements to this imaging setup will include optics to support OH, CH and CH_2O PLIF imaging to provide evidence of the low-temperature reactions ahead of the flame front and experimental validation of the results presented in §3.4.

3.3. Flame propagation rate measurements and EGAI sensitivity

Flame propagation rate measurements for index 1 experiments that featured piston offsets of less than 5.00 ms are listed in Table 2 with their corresponding measured pressures and estimated temperatures at the time of ignition. Only experiments conducted using a single set of initial conditions (index 1) are presented to eliminate the effects of changing inert composition and gas density on diffusivity and propagation rates.

Flame propagation rate was found to correlate most strongly with piston offset (Spearman rank correlation coefficient, $\rho = 0.621$), as depicted in Fig. 12. Propagation rate was not as strongly correlated with temperature at ignition ($\rho = 0.221$), pressure at ignition ($\rho = 0.275$), and ON ($\rho = 0.239$) over the ranges tested. A detailed account of how propagation rate was

Table 2
Unburned flame propagation rate measurements listed by their mean and standard deviations for the index 1 experiments (initial conditions: 300 K and 1.000 bar; oxidizer/inert molar composition: 21% O_2 / 79% N_2; stoichiometric). Only the experiments with piston offsets of less than 5.00 ms are included to ensure that the effect of turbulence is minimized. The number of measurements is included to indicate the level of confidence in the data. The "Simulated LFS" column features the predicted laminar flame speeds from the 1-D CHEMKIN simulations with 590 K and 22.5 bar ambient conditions.

PRF	# of Data Points	Temp. (K)	Pressure (bar)	Measured Prop. Rate (cm/s)		Simulated LFS (cm/s)
				Mean	SD	(590 K, 22.5 bar)
50	6	571 ± 2	22.0 ± 0.2	63.3	15.0	52.5
60	4	598 ± 5	22.9 ± 0.2	80.3	6.3	51.1
70	1	614	23.8	83.5	–	50.4
75	4	605 ± 4	23.1 ± 0.2	62.5	4.1	50.2
80	3	591 ± 1	22.6 ± 0.0	65.1	10.5	49.7
90	3	612 ± 3	23.2 ± 0.1	63.3	13.9	49.2
100	5	589 ± 3	22.5 ± 0.2	65.1	8.3	48.5

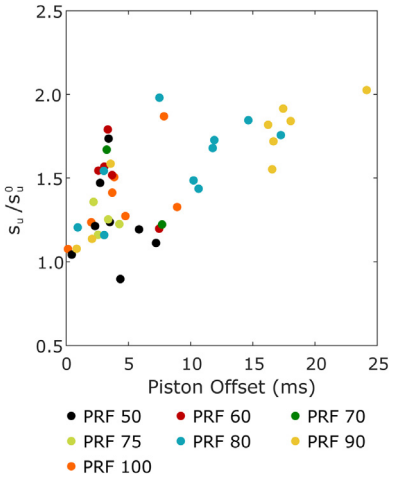

Fig. 12. Unburned, zero-stretch flame propagation rates, s_u, normalized by simulated laminar flame speed s_u° for all experimental conditions listed in Table 2. The results are plotted against measured piston timing offset. Fuel octane number is signified by symbol color. (For interpretation of the references to color in this figure legend, the reader is referred to the web version of this article.)

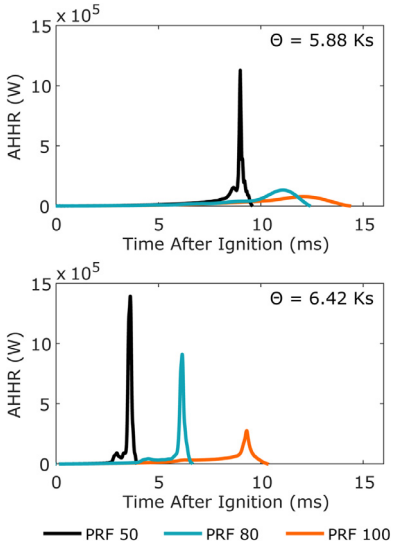

Fig. 13. Simulated AHRR signatures for PRF 50, 80, and 100 under the 5.88 Ks and 6.42 Ks temperature history conditions.

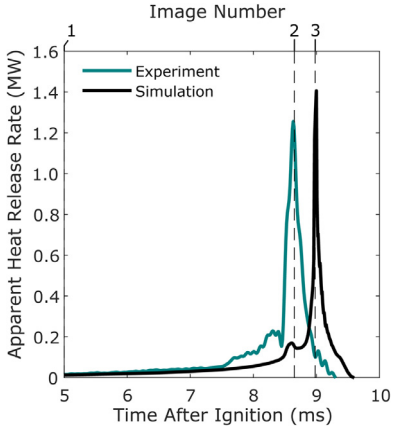

Fig. 14. AHRR profiles for the experimental and simulated PRF 50, index 1 test condition. The time-integrated temperature, Θ, for the experiment and simulation are 6.28 Ks and 5.88 Ks, respectively. The times at which the simulation images of Fig. 15 are taken are indicated by the dashed vertical lines.

influenced by temperature, pressure, turbulence, and fuel reactivity can be found in SI §S2.3. Note that the measured flame propagation rate was not expected to vary strongly with octane number for PRF fuels and fixed upstream conditions because laminar flame speed does not vary strongly with octane number under these conditions as indicated by the simulated laminar flame speed results also included in Table 2. The experimental results were consistent with these expectations.

Moreover, as shown in Fig. 12, the measured flame propagation rates approached the calculated 1-D laminar flame speed predictions as piston offset approached 0.0 ms. Though highly encouraging, this result does not conclusively prove that the opposed-piston RCM in its current configuration represents a viable approach for fundamental measurements of laminar flame speed. Even at very low piston offset and presumed lower levels of turbulence (for example, as shown in Fig. 10), the flames observed in this study feature multi-lobed cellular structures. Given that the observed cellular structures are steady as the flame propagates, it is unlikely that they are caused by hydrodynamic instabilities [34], but instead by the initial multi-lobed shape of the plasma created by the focused laser [35]. While the literature suggests that the laser spark provides an initial boost to the flame front due to plasma expansion and heat transfer, its influence over flame propagation rate once the flame has fully developed is minimal [34, 36]. However, the cellular artifacts of the initial flame kernel likely affect flame propagation to a degree proportional to their size [36] and, therefore, the flames observed in this apparatus deviate from true laminar flames (i.e. steady, adiabatic planar, stretch-free, and one dimensional [37]. The observed agreement between measured flame propagation rates and the calculated 1-D laminar flame speed in-

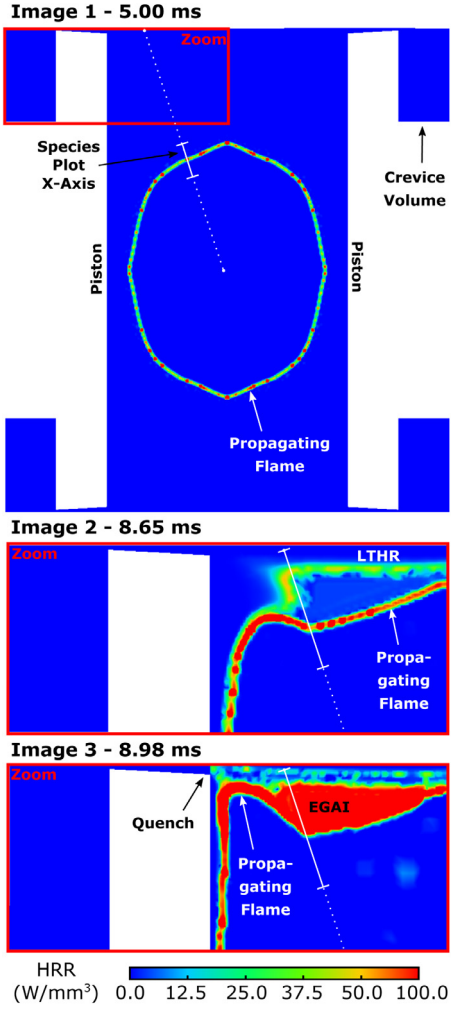

Fig. 15. (Above) Colorized isocontours of volumetric heat release rate (W/mm^3) at the central plane of the RCM combustion chamber with pistons in the TDC position. The piston cross-sections are shown in white. Images 2 and 3 are enlarged to better visualize the LTHR and EGAI in the region outlined in red in Image 1. Species and temperature measurements taken across the white dotted lines are presented in Fig. 16. The x-axes bounds of the corresponding species plots are represented by the bracketed solid line overlays in each image. (For interpretation of the references to color in this figure legend, the reader is referred to the web version of this article.)

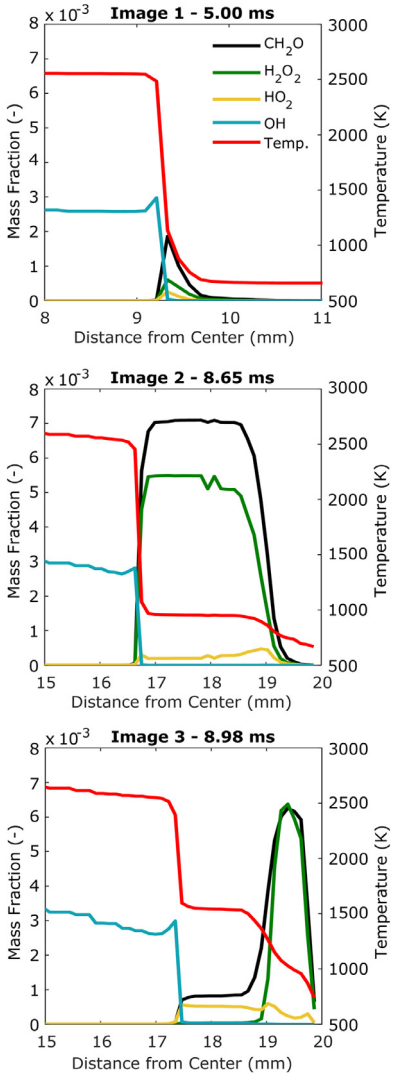

Fig. 16. (Right) The species and temperature profiles corresponding with images 1, 2, and 3 in Fig. 15. The profiles were taken along the dotted line that extends from the center of the chamber to the wall in image 1. The extent of the x-axis for each plot is represented by the solid white line in the corresponding image. The bracket closest to the center represents the lower limit of the x-axis and the bracket furthest from the center represents the upper limit of the x-axis.

stead (a) suggests that the experimental results with low piston timing offset result in near-quiescent post-compression flowfields along the combustion chamber stagnation plane that produce propagating flames with low turbulence, and (b) illustrates the potential of the experimental methods described herein as a means to measure flame propagation rates at elevated pressures and elevated unburned gas temperatures for experimental trials with near-symmetric compression.

3.4. Computational results

The AHRR profiles from simulations performed for PRF 50, 80, and 100 at time-integrated temperatures of 5.88 Ks and 6.42 Ks are shown in Fig. 13. As observed in the experiments, the magnitude of the maximum AHRR varied monotonically with fuel blend reactivity and time-integrated temperature. For both time-integrated temperature conditions, the lower reactivity (PRF100) blends produce a longer combustion duration with lower rate of increase in AHRR compared to the more reactive blends (PRF50 and PRF 80). The AHRR profiles for the simulations with time-integrated temperature of 6.42 Ks exhibit the same general signatures observed in the experiments. Specifically, the simulated AHRR profiles show the initial heat release from the propagating flame, followed by an initial peak from low temperature heat release in the end-gas upstream of the propagating flame and the large peak from EGAI. For a time-integrated temperature of 5.88 Ks, the PRF 50 case exhibit these behaviors, whereas the PRF 80 and PRF 100 cases do not result in EGAI.

A representative experimental AHRR profile for the PRF50, index 1 test condition is presented along with its corresponding simulation in Fig. 14. The time-integrated temperature values for the experiment and simulation were 6.28 Ks and 5.88 Ks, respectively. In contrast to the low, but finite, piston offset of 2.189 ms measured during the experiment, the simulation assumed perfectly symmetrical compression (piston offset of 0 ms) due to the symmetrical boundary condition at the centerline of the 1/8th sector computational domain. Qualitative agreement between the AHRR profiles was achieved despite the slightly lower time-integrated temperature and presumed lower level of bulk fluid motion in the simulation due to symmetry. The experimentally measured and predicted flame propagation rates were 42.5 cm/s and 41.9 cm/s,

respectively. Agreement between these flame propagation rates was also evident based on the similar slopes of the AHRR curves between 0.0 and 7.5 ms. The experimental and simulated f_{EGAI} measurements were 0.312 and 0.346, respectively. The similarity of the AHRR profiles suggests analogous behavior in the three observed combustion modes (propagating flame, LTHR and EGAI), which suggests that combined experimental and modeling approach employed herein can be an effective means of examining the underlying phenomena that govern knock propensity in spark ignited engines.

Colorized isocontours of volumetric heat release rate (W/mm^3) through the central plane of the combustion chamber for PRF50 and time-integrated temperature of 5.88 Ks are shown in Fig. 15 at t = 5.00 ms, 8.65 ms and 8.98 ms after ignition (as denoted by the vertical dashed lines in Fig. 14). These times were selected for their concurrence with the characteristic AHRR behavior used to identify propagating flames, LTHR, and EGAI events. The field of view in these frames reveals the piston cross-sectional profiles along with the crevice volumes situated on the backside of each piston face. Image 1, captured 5.00 ms after ignition, depicts a near-spherical flame front propagating away from the central ignition site. As the flame approaches the chamber wall several milliseconds later, low temperature heat release is observed in the corner end-gas as indicated by the light green region in Image 2. Shortly thereafter, volumetric EGAI ensues (Image 3). The forced quench condition in the crevice volume is evident by the abrupt decrease in heat release rate observed at the entrance of the crevice channel.

Fig. 16 presents radical (OH, HO_2) and intermediate (H_2O_2, CH_2O) species and temperature profiles as a function of distance through the center plane of the three heat release isocontour images in Fig. 15. The species and temperature profiles are taken along the dotted line that extends from the center of the chamber to the wall, angled such that the LTHR and EGAI events are captured. In Image 1, species and temperature profiles are consistent with expectations for the convective-diffusive preheat zone of a propagating flame. As the flame approaches the wall and low-temperature chemistry becomes active, substantial amounts of formaldehyde (CH_2O) and hydrogen peroxide (H_2O_2) are produced, along with a modest rise in temperature (Image 2 – 8.65 ms). Both the flame surface and thermal boundary layer at the RCM cylinder wall can be identified in the Image 2 plot by the steep decrease in radical species on either side of the end-gas volume. The volumetric formaldehyde production is indicative of low-temperature n-alkane chemistry. Hydrogen peroxide production is indicative of high-pressure hydrogen chemistry and leads to the chain branching thermal decomposition reaction HOOH+M→OH+OH+M [38]. These autoignition precursor species are more stable at medium temperatures than the reactants that formed them, and as such, temporarily slow the volumetric reactions to produce a two-stage ignition effect. Indeed, after a slight delay, the low-temperature heat release rapidly transitions into a strong volumetric heat release that constitutes EGAI (Image 3 – 8.98 ms). During the transition to EGAI, the hydrogen peroxide mass fraction increases further and then dramatically decreases due to the thermal decomposition reaction. In this case, EGAI does not immediately break through the thermal boundary layer and the higher concentrations of formaldehyde and hydrogen peroxide remain a short while longer.

Similar end-gas combustion phenomena were observed for the simulated PRF 80 case with time-integrated end-gas temperature of 5.88 Ks and for all of the simulations performed with time-integrated temperature of 6.42 Ks. For PRF 100 with time-integrated temperature of 5.88 Ks, no volumetric hydrogen peroxide or formaldehyde production, and no LTHR or EGAI events were predicted. Lastly, the simulated end-gas autoignition fraction, f_{EGAI}, is plotted against ON in Fig. 9 for time-integrated temperature of 5.88 Ks and 6.42 KS, respectively, for comparison against experimental results under similar conditions. The simulated results for end-gas autogintion fraction as a function of ON exhibit similar behavior to that observed in the experiments, although the simulations overpredict the end-gas autoignition fraction for a given time-integrated temperature.

Conclusions

The results of this study demonstrate the ability to evaluate knock propensity of SI fuels by observation of EGAI in the unburned gasses upstream of laser-ignited, premixed flames in an RCM at engine-relevant pressures and temperatures. To demonstrate this technique, stoichiometric PRF blends of varying reactivity ($50 \leq$ PRF ≤ 100) were ignited over a range of temperatures and pressures, all in excess of 545 K and 16.1 bar, which produced outwardly propagating flames. High-speed pressure measurements, paired with schlieren imaging, clearly indicated the presence of EGAI for PRF blends. The magnitude of the EGAI event, as quantified by the fraction of the total heat release contributed by EGAI, increased with fuel reactivity. The results were also affected by variation in the level of bulk fluid motion in the RCM combustion chamber after compression due variation in timing between the two pistons.

Experiments were accompanied by time-dependent, three-dimensional computational modeling with detailed chemical kinetics performed using CONVERGE^{TM}. The model results for stoichiometric PRF 50 fuel in an 11.9% CO_2 /67.1% N_2 /21.0% O_2 oxidizing environment revealed the presence of low-temperature heat release and hydrogen peroxide and formaldehyde formation in the end-gas upstream of the propagating flame. Low-temperature heat release increased the temperature and degree of chain branching in the end-gas and ultimately led to EGAI. The model results for the PRF 100, Θ = 5.88 Ks case exhibited neither low temperature heat release nor hydrogen peroxide formation in the end-gas, and EGAI did not occur.

The methods presented herein represent a proof-of-concept that the effects of fuel reactivity and time-integrated end-gas temperature on a fuel's knock propensity can be quantified in an SI RCM. RCM systems currently in operation vary substantially between research groups in their design, operation, and combustion chamber geometry. Therefore, development of a standardized test method to quantify knock propensity will require the standardization of equipment and operating procedure (e.g., piston compression timing, spark timing, bore/stroke, compression ratio, wall temperatures). The development of such standards would result in the ability to quantify knock propensity using much lower quantities of fuel in comparison to existing ASTM test methods that rely on CFR engine testing. This would be advantageous for screening the knock propensity of novel alternative fuels that are often prohibitively expensive to produce in large quantities. Further, with increased control over end-gas temperature and pressure in comparison to engine testing, the RCM experiments have the potential to provide a better understanding of the underlying physics of knock propensity and octane index sensitivity via optical measurements of the propagating flame front and direct measurements of intermediate species in the end-gas (e.g., H_2O_2 and CH_2O) prior to the onset of EGAI.

Declaration of Competing Interest

The authors declare that they have no known competing financial interests or personal relationships that could have appeared to influence the work reported in this paper.

Acknowledgements

This work was supported by the Department of Energy [Grant No. DE-EE0008331].

Supplementary materials

Supplementary material associated with this article can be found, in the online version, at doi:10.1016/j.combustflame.2021.111661.

References

[1] J.B. Heywood, Internal Combustion Engine Fundamentals, McGraw-Hill, New York, 1988.
[2] Z. Wang, H. Liu, R.D. Reitz, Knocking combustion in spark-ignition engines, Prog Energy Combust Sci 61 (2017) 78–112.
[3] ASTM D2700-12: standard test method for motor octane number of spark-ignition engine fuel, (2018).
[4] ASTM D2699-12: standard test method for research octane number of spark-ignition engine fuel, (2018).
[5] D03 Committee, Standard Practice for Determining the Calculated Methane Number (MNC) of Gaseous Fuels Used in Internal Combustion Engines, ASTM International, n.d. (2018).
[6] W.G. Lovell, Knocking characteristics of hydrocarbons, Ind. Eng. Chem. 40 (1948) 2388–2438.
[7] G.T. Kalghatgi, Fuel anti-knock quality - part i. engine studies, SAE Int. (2001).
[8] G.T. Kalghatgi, Fuel Anti-Knock Quality- Part II. Vehicle Studies - How Relevant is Motor Octane Number (MON) in Modern Engines?, SAE International, 2001.
[9] G.T. Kalghatgi, Developments in internal combustion engines and implications for combustion science and future transport fuels, Proc. Combust. Inst. 35 (2015) 101–115.
[10] J.F. Griffiths, P.A. Halford-Maw, C. Mohamed, Spontaneous ignition delays as a diagnostic of the propensity of alkanes to cause engine knock, Combust. Flame 111 (1997) 327–337.
[11] A.A. Attar, G.A. Karim, Knock Rating of Gaseous Fuels, J Eng Gas Turbine Power 125 (2003) 500.
[12] D02 Committee, Test Method for Determination of Octane Number of Spark-Ignition Engine Fuels by On-Line Direct Comparison Technique, ASTM International, n.d. (2021).
[13] M. van Essen, A new method for characterizing the knock resistance for gaseous fuels, (2014).
[14] D02 Committee, Test Method for Determination of Derived Cetane Number (DCN) of Diesel Fuel Oils Ignition Delay and Combustion Delay Using a Constant Volume Combustion Chamber Method, ASTM International, n.d, 2017.
[15] D02 Committee, Test Method for Determination of Ignition Delay and Derived Cetane Number (DCN) of Diesel Fuel Oils by Combustion in a Constant Volume Chamber, ASTM International, n.d. (2021).
[16] V.N. Korolev, A.V. Marugin, Determination of the octane number of a fuel by the IR spectroscopy method, J. Appl. Spectrosc. 67 (2000) 336–342.
[17] S. Gersen, M. van Essen, H. Levinsky, G. van Dijk, Characterizing gaseous fuels for their knock resistance based on the chemical and physical properties of the fuel, SAE Int. J. Fuels Lubr. 9 (2016) 1–13.
[18] S. Gersen, M.H. Rotink, G.H.J. Van Dijk, H. Levinsky, A new experimentally tested method to classify gaseous fuels for knock resistance based on the chemical and physical properties of the gas, 2011.
[19] H. Hu, J. Keck, Autoignition of adiabatically compressed combustible gas mixtures, 872110, 1987.
[20] R. Lawson, F.Egolfopoulos Robert, Autoignition of reacting mixtures at engine-relevant conditions using confined spherically expanding flames, Proc. Combust. Inst. (September 2020).
[21] C. Dumitrache, M. Baumgardner, A. Boissiere, A. Maria, J. Roucis, A.J. Marchese, A. Yalin, A study of laser induced ignition of methane–air mixtures inside a rapid compression machine, Proc. Combust. Inst. 36 (2017) 3431–3439.
[22] C. Liu, G. Suo, A rapid compression machine study of autoignition, spark-ignition and flame propagation characteristics of H2/CH4/CO/air mixtures, Combust. Flame 188 (2018) 150–161.
[23] A. Zdanowicz, End-Gas Autoignition Propensity and Flame Propagation Rate Measurements in Laser-Ignited Rapid Compression Machine Experiments, Colorado State University, 2019.
[24] S. Bhoite, A Computational Study of Autoignition, Spark Ignition and Dual Fuel Droplet Ignition in a Rapid Compression Machine, Colorado State University, 2017.
[25] Y. Qi, Z. Wang, J. Wang, X. He, Effects of thermodynamic conditions on the end gas combustion mode associated with engine knock, Combust. Flame 162 (2015) 4119–4128.
[26] P. Pal, T. Lu, Multidimensional numerical simulations of knocking combustion in a cooperative fuel research engine, J. Energy Resour. Technol. (2018).
[27] O. Nyong, R. Woolley, S. Blakey, E. Alborzi, Optimal piston crevice study in a rapid compression machine, IOP Conf. Ser.: Mater. Sci. Eng. 243 (2017) 012018.
[28] C.J. Sung, H. Curran, Using rapid compression machines for chemical kinetics studies, Prog. Energy Combust. Sci. 44 (October 2014) 1–18.
[29] A. Boissiere, Effect of Additives on Laser Ignition and Compression Ignition of Methane and Hydrocarbons in a Rapid Compression Machine, Master of Science, Colorado State University, 2016.
[30] J. Livengood, P. Wu, Correlation of autoignition phenomena in internal combustion engines and rapid compression machines, Symp. (Int.) Combust. (1955) 347–356.
[31] M.W. Chase, NIST-JANAF thermochemical tables, J. Phys. Chem. Ref. Data. Monograph 9 (1998) 1–1951.
[32] A.P. Kelley, C.K. Law, Nonlinear effects in the extraction of laminar flame speeds from expanding spherical flames, Combust. Flame 156 (2009) 1844–1851.
[33] C.K. Law, Combustion Physics, Cambridge University Press, Cambridge ; New York, 2006.
[34] E. Groff, The cellular nature of confined spherical propane-air flames, Combust. Flame 48 (1982) 51–62.
[35] D. Bradley, R. Woolley, Fundamentals of high-energy spark ignition with lasers, Combust. Flame 138 (1–2) (2004) 55–77.
[36] D. Bradley, C.M. Harper, The development of instabilities in laminar explosion flames, Combust. Flame 99 (3–4) (1994) 562–572.
[37] E. Varea, Experimental Analysis of Laminar Spherically Expanding Flames, INSA de Rouen, 2013.
[38] I. Glassman, R.A. Yetter, N. Glumac, Combustion, 5th edition, Academic Press, Waltham, MA, 2015.